

Non-intrusive estimation of the buffet loads on a supercritical airfoil with SCBs

D'Aguanno, A.; Corduas, A.; Schrijer, F. F.J.; van Oudheusden, B. W.

DOI

[10.1007/s00348-025-04000-5](https://doi.org/10.1007/s00348-025-04000-5)

Publication date

2025

Document Version

Final published version

Published in

Experiments in Fluids

Citation (APA)

D'Aguanno, A., Corduas, A., Schrijer, F. F. J., & van Oudheusden, B. W. (2025). Non-intrusive estimation of the buffet loads on a supercritical airfoil with SCBs. *Experiments in Fluids*, 66(4), Article 80. <https://doi.org/10.1007/s00348-025-04000-5>

Important note

To cite this publication, please use the final published version (if applicable). Please check the document version above.

Copyright

Other than for strictly personal use, it is not permitted to download, forward or distribute the text or part of it, without the consent of the author(s) and/or copyright holder(s), unless the work is under an open content license such as Creative Commons.

Takedown policy

Please contact us and provide details if you believe this document breaches copyrights. We will remove access to the work immediately and investigate your claim.



Non-intrusive estimation of the buffet loads on a supercritical airfoil with SCBs

A. D'Aguanno¹ · A. Corduas¹ · F. F. J. Schrijer¹ · B. W. van Oudheusden¹

Received: 5 September 2024 / Revised: 10 February 2025 / Accepted: 13 February 2025
© The Author(s) 2025

Abstract

This study experimentally investigates the effect of three-dimensional shock control bumps (SCBs) on the aerodynamic loads of a supercritical airfoil under transonic buffet conditions. The experiments consisted in planar particle image velocimetry (PIV) measurements and have been carried out in the transonic-supersonic wind tunnel of TU Delft under fully developed buffet conditions ($Ma = 0.7$ and $\alpha = 3.5^\circ$). The bumps are wedge-shaped and have been placed in the center of the shockwave oscillation range. Shock detection and phase-averaged velocity fields confirm that properly designed and spaced ($\Delta y_{SCB}/c = 25\%$) SCBs reduce the shockwave oscillation range (compared to the clean case). The velocity data have been further used to evaluate the pressure field around the entire airfoil, and afterward, lift and drag coefficients have been retrieved, respectively, from momentum contour and wake integral approaches. Results demonstrate that SCBs have a beneficial effect on the aerodynamic loads with an increase in lift and a decrease in drag under fully developed buffet conditions. More importantly, a strong reduction of the amplitude of oscillations of both lift and drag coefficient, within the different buffet phases, was noted. Tests at multiple spanwise locations revealed relevant differences, with lower drag and higher lift values being achieved in the symmetry plane of a SCB, while a worse performance (with values comparable to the clean case) was achieved in the symmetry plane in between two adjacent bumps.

1 Introduction

Transonic buffet is one of the limiting factors for the flight envelope of modern civil aircraft. Among the first researchers to study this phenomenon, Hilton and Fowler (1952) distinguished between two typologies of transonic buffet: Type I which occurs under nominally symmetric conditions on both pressure and suction side (typical on biconvex sections) and Type II which occurs on supercritical airfoils with shock oscillation only on the upper surface at nonzero angles of attack. Since the latter is characteristic of operative conditions in modern aircraft, this is the topic of the current study. First investigations of this type of shockwave movement were reported by Pearcey (1955) and Tijdeman (1977), while a first physical description of this phenomenon was proposed by Lee (1990), who described the shockwave oscillation as being the result of a feedback mechanism sustained by the

propagation of downstream vortices from the shockfoot and the consequent generation of upstream traveling pressure waves at the trailing edge of the wing. The nature and the characteristics of the upstream traveling pressure waves have received significant attention in the last decade (see Hartmann et al. (2013); Garnier and Deck (2010); Jacquin et al. (2009) and D'Aguanno et al. (2021b)) providing a significant improvement of Lee's original model. An alternative view on buffet was given by Crouch, who described it as a consequence of a global flow instability (see Crouch et al. (2007) and Crouch et al. (2019)) with the results of this analysis predicting the buffet onset as a function of Ma and α and showing good agreement with experimental data.

The interaction of transonic buffet with the aerodynamic surfaces of an aircraft could lead to structural vibration (referred to as buffeting), potentially resulting in fatigue failure. It is therefore not surprising that transonic buffet was found to strongly limit the performance of the first aircraft experiencing (near-)sonic conditions in the 1940 s and 1950 s and led to some fatal accidents (Meier (2010)). Nowadays, the regulation work of flight authorities has ensured that catastrophic consequences as a result of transonic buffet are avoided, by imposing a 0.3 g margin with respect to

✉ A. D'Aguanno
A.Daguanno@tudelft.nl

¹ Aerodynamics Section, Department of Flow Physics and Technology, Delft University of Technology, Kluyverweg 2, 2629HS Delft, The Netherlands

the transonic buffet onset (Piccola (2012)). Transonic buffet could become even more limiting for future generation aircraft, as they are increasingly characterized by light and flexible wings and therefore more sensitive to buffeting loads.

To reduce the effect of this undesirable phenomenon on the flight envelope, active and passive control systems can be used as described in the review paper of Giannelis et al. (2017)). Active control systems demonstrated to be efficient in controlling transonic buffet, capable of completely eliminating the shockwave oscillation; however, they generally require a complicated (and a relatively heavy) actuation system (Caruana et al. (2003a); Ren et al. (2020)). Thus, in applications where simplicity and robustness have a preference, passive control system is implemented. These control systems are typically located either in the separated area (vortex generators or fluidic vortex generators as in Caruana et al. (2003b) and Brion et al. (2019)) or in the trailing edge area (e.g., trailing edge flaps, see Lee (1992); Despre et al. (2001); D'Aguanno et al. (2022)) or in proximity of the shockwave oscillation range (shock control bumps, see Bruce and Colliss (2015)), with the goal of directly stabilizing the shock position or the extent of the separated area.

In this study, shock control bumps (SCBs) will be investigated in more detail. This typology of control devices has been used in various applications, such as for the control of shockwave boundary layer interaction (Bruce and Colliss (2015)); for the control of transonic flows on airfoil and wings (Ogawa et al. (2008)); and also as a flow control device in supersonic engine intakes (Babinsky and Ogawa (2008)). For steady transonic applications the crest of the shock control bump should be located in correspondence of the shockwave position, since upstream or downstream locations of the SCB could lead to a re-expansion of the flow and the occurrence of secondary shockwave structures (Bruce and Colliss (2015)). To reduce the occurrence of these detrimental effects in off-design conditions, three-dimensional (3D) SCBs are typically preferred over two-dimensional (2D) SCBs (i.e., spanning the entire wing span). 3D SCBs have two major working principles, firstly, by virtue of the formation of a λ -shockwave instead of the traditional quasi-normal shockwave (induced by the front ramp of the SCB) and, secondly, the promotion of a localized region of attached flow in view of the generation of streamwise vortices from the side flanks of the bump.

In recent years 3D SCBs have been applied to control transonic buffet as, for example, in the studies of Eastwood and Jarrett (2012) and Tian et al. (2017), achieving in both cases a stabilization of the shockwave oscillation. However, the effectiveness of these devices is not univocal, with the numerical investigation of Bogdanski et al. (2014) showing detrimental effects of 3D SCBs on the buffet onset and amplitude. Geoghegan et al. (2020) demonstrated that although the effectiveness of SCBs depends on several

parameters, for buffet control they appear to be less sensitive to their streamwise location than for steady shockwave applications, with reduction of the buffet unsteadiness being achieved when the SCB crest is located within $\pm 5\%c$ with respect to the average shockwave location. Another relevant aspect which affects the performance of 3D SCBs is the spacing between adjacent devices. As shown by the study of Ogawa et al. (2008), in the presence of 3D SCBs the leading edge oblique shockwaves of adjacent bumps wrap around the corresponding SCB and are partially overlapping. The spacing of SCBs is a crucial parameter which determines whether this interaction is detrimental or beneficial, as shown by the particle image velocimetry data (PIV) of D'Aguanno et al. (2023), which reported an optimization of the SCB performance for a spanwise spacing $\Delta y_{SCB} = 25\%c$. In the same study, it was observed that the spacing parameter, through its effect on the production of vortices from the tail of the bumps, also influences the drag reduction working principle of a SCB.

Although several studies have suggested that SCBs are effective in reducing transonic buffet oscillations (Giannelis et al. (2017)), their effect on the mean flow and aerodynamic loads should still be quantified. In numerical studies, these loads can be directly obtained from the pressure information, as in the study of Geoghegan et al. (2020) who reported an increase of 5-10% of the lift-to-drag ratio in the presence of properly placed SCBs. A detailed investigation of the effect of SCBs on lift and drag is also given in the numerical study of Eastwood and Jarrett (2012) who investigated SCBs with different widths, spacing and edge design for both steady and unsteady applications, obtaining increases in lift-to-drag ratio of about 10%. Differently, in experimental studies the evaluation of aerodynamic loads in the presence of SCBs is very scarce and mainly confined to direct pressure measurements in localized regions of the model (see Milholen and Owens (2005) as an example). Additionally, in the presence of pressure orifices on the model, flush mounting SCBs on the suction side of the airfoil will make lift estimation impractical (Konig et al. (2009)), unless complicated models implemented with fixed SCBs and distributed pressure taps are designed. Moreover, the spatial resolution of pressure taps is commonly not sufficient to analyze the flow structures associated with the presence of SCBs. A possible alternative is the use of pressure sensitive paint (PSP), which has already been used in similar applications by Konig et al. (2009) and Bruce and Babinsky (2012). However, although PSP allows to visualize surface pressure structures along the entire object of interest, it is not possible to obtain information on the flow features which are causing them.

These limitations can be overcome by means of a load estimation procedure based on velocity data from PIV. The advantages of this methodology are associated with the simplicity of the experimental models, the non-intrusivity

of the technique and the high spatial resolution of the extracted pressure data (Raffel et al. (2018)). Nevertheless, this pressure determination is associated with higher uncertainties when compared to more classical, direct pressure evaluation methods that rely on wall-mounted sensors in view of the required validity of the underlying hypothesis, as well as the propagation of the uncertainty from the velocity measurements (Ragni et al. (2009)). Applications for pressure reconstruction from PIV data for both incompressible and (more recently) compressible applications are widespread as shown by the review articles of van Oudheusden (2008) and van Oudheusden (2013). In Ragni et al. (2009), time-averaged lift and drag have been estimated from PIV measurements around a NACA 0012 for high subsonic conditions ($Ma = 0.6$) and compared to surface pressure transducers and wake rake measurements, showing very good agreement.

The goal of this study is to use an analogous pressure reconstruction approach to the one of Ragni et al. (2009) to provide a quantitative characterization of the buffet loads and to assess the impact of the SCB control on this load behavior. Although several other studies have previously applied pressure reconstruction procedures to PIV data in compressible conditions—such as Tagliabue et al. (2017); Liu et al. (2017), and, more recently Lagemann et al. (2024) for transonic buffet—this study will consider both the time-averaged loads and their phase-wise variation over the transonic buffet cycle.

2 Methodology

2.1 Experimental methods

2.1.1 Wind tunnel and model

The experiments of this study were carried out in the transonic-supersonic blowdown wind tunnel of TU Delft, the TST-27. The wind tunnel has a rectangular test section which is 25.5 cm high and 28 cm wide. Transonic Mach numbers are achieved using a transonic choke mechanism located downstream of the test section, obtaining a Mach number precise to the third decimal digit. All the experiments were carried out with a freestream Mach number $Ma_\infty = 0.7$, a total pressure $p_{0\infty} = 200$ kPa and a total temperature $T_{0\infty} = 288$ K. These settings resulted in a freestream pressure $p_\infty = 144$ kPa and a freestream temperature $T_\infty = 262$ K. The main flow conditions are summarized in Table 1 with the relative measurement uncertainties, with the resulting uncertainty in the freestream velocity being approximately 0.2 m/s, corresponding to about 0.1% of the freestream value.

Table 1 Free stream flow conditions

Parameter	Symbol	Value	Unit
Mach number	Ma_∞	0.7000 ± 0.0005	
Velocity	V_∞	227.2 ± 0.2	m/s
Total pressure	$p_{0\infty}$	200.0 ± 0.5	kPa
Total temperature	$T_{0\infty}$	288.0 ± 0.5	K

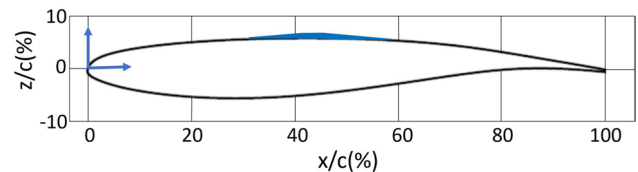


Fig. 1 OAT15A airfoil with wedge SCB mounted on the suction side

The experimental model which has been used in this study is extruded from the OAT15A airfoil (see Fig. 1), and it is clamped to both sides of the wind tunnel. This supercritical airfoil has been designed by ONERA and having been used in several numerical (Garnier and Deck (2010); Grossi et al. (2014); Szubert et al. (2015), and Huang et al. (2012)) and experimental (Jacquin et al. (2009); D'Aguanno et al. (2021a) and Accorinti et al. (2022)) studies, it is commonly considered a benchmark airfoil for transonic buffet studies. The model has a chord (c) of 10 cm, a span (b) of 28 cm, a maximum thickness-to-chord ratio of 12.3% and a trailing edge thickness of $0.75\%c$. To ensure a fully turbulent boundary layer in the shockwave oscillation range, a transition trip with a streamwise width of $2\%c$ has been attached at $x/c = 0.07$ of the chord on the suction side of the model. The transition trip has been realized with Carborundum particles (particle size of 0.0139 mm). Transition trips of similar dimensions and locations have been also used in other experimental studies, such as in Jacquin et al. (2009); Feldhusen-Hoffmann et al. (2021) and D'Aguanno et al. (2021a).

The wind tunnel model has been tested at an angle of attack of 3.5° and a Mach number of 0.7 (Reynolds number based on chord $Re_c = 2.62 \cdot 10^6$), conditions for which fully developed buffet oscillation has been observed on the same model (see D'Aguanno et al. (2021a)). These flow conditions are uncorrected for wind tunnel model blockage; however, using empirical correction factors derived for the same wind tunnel in similar conditions (Bannink and Bakker (1983)), a corrected Mach number of 0.73 is computed. This value is in agreement with the Mach number obtained by Jacquin et al. (2009) for fully developed transonic buffet.

The SCBs which have been used in this study are wedge-shaped and are based on the design of Colliss et al. (2016) and Mayer et al. (2018) and are the same SCBs which have

been investigated in a previous study in the same wind tunnel (D'Aguanno et al. (2023)). A schematic with the exact dimensions of the SCB is shown in Fig. 2 (right). The SCBs have been placed with their crest located at $x/c = 45\%c$, which is in proximity of the average shockwave position for the clean airfoil. The SCBs have been flush-mounted on the airfoil with a double side tape of $0.13\%c$ thickness. As a result, the overall vertical distance of the SCB crest with respect to the airfoil surface is $0.9\%c$, which is equal to the estimated local boundary layer thickness, evaluated for an equivalent flat plate. As suggested by D'Aguanno et al. (2023), the SCBs have been placed with a spanwise spacing of $25\%c$ (as shown in Fig. 2, left) to optimize their control performance. The main model and SCB parameters are summarized in Table 2.

2.1.2 Experimental setup

During the wind tunnel tests, low-speed planar PIV measurements were performed, and for this purpose a LaVision sCMOS 5MP camera (resolution of $2560 \text{ px} \times 2160 \text{ px}$) was used and fitted with a 105 mm lens with an f-stop of 8. To evaluate the aerodynamic loads, velocity data around the complete airfoil are needed (suction and pressure sides), therefore, two sets of measurements were conducted for each

test case, with the airfoil being flipped upside down in the second measurement. In Fig. 3 FOV_1 refers to the field of view of the first set of measurements and FOV_2 to the second. The combined FOV extends around the entire airfoil in a streamwise-vertical oriented FOV from roughly $20\%c$ upstream of the airfoil up to $20\%c$ downstream of the trailing edge and vertically from $z/c = -60\%$ to $z/c = 60\%$. Therefore, it is worth noting that with respect to D'Aguanno et al. (2023), in this study, a characterization of the full velocity field around the airfoil is provided, instead of only (part of) the suction side domain.

For the clean configuration, the flow field can be considered 2D (see D'Aguanno et al. (2021b) for more details); therefore, the loads evaluated at a particular measurement plane are representative of the loads on the entire model; this is, however, not the case for the shock control bump configuration. To account for the spanwise variation of the loads, the PIV measurements have been repeated at three different spanwise measurements planes (see Fig. 2, left):

- in correspondence of the centerline of the central bump ($y/c = 0$);
- for $y/c = \Delta y_{SCB}/4 = 6.25\%$;
- for $y/c = \Delta y_{SCB}/2 = 12.5\%$ (at half distance between two consecutive bumps).

For each set of measurements 700 images have been taken, in 2 runs of 350 images each (23.6 s of acquisition time per test).

To compute the velocity field, DEHS seeding particles have been used. These particles have a median particle size of $1 \mu\text{m}$ and in a previous investigation demonstrated to have a good flow-tracing performance with a relaxation time of $2 \mu\text{s}$ (see Ragni et al. (2011)). The seeding particles in the measurement planes were illuminated by a Quantel Evergreen 200 dual cavity laser, with an acquisition frequency of 15 Hz and with a pulse separation $dt = 3 \mu\text{s}$. By using a light optics probe, a laser sheet with a thickness of

Table 2 Model and SCB parameters

Parameter	Symbol	Value	Unit
Airfoil chord	c	0.1	m
Airfoil span	b	0.28	m
Angle of attack	α	3.50 ± 0.05	$^\circ$
Reynolds number based on c	Re_c	$(2.62 \pm 0.01) \cdot 10^6$	
SCB height	h	$0.77 (+0.13; \text{tape})$	$\%c$
SCB length	l	28	$\%c$
SCB crest position	x_{SCB}	45	$\%c$
SCB spacing	Δy_{SCB}	25	$\%c$

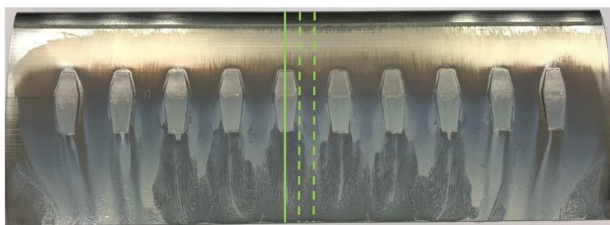
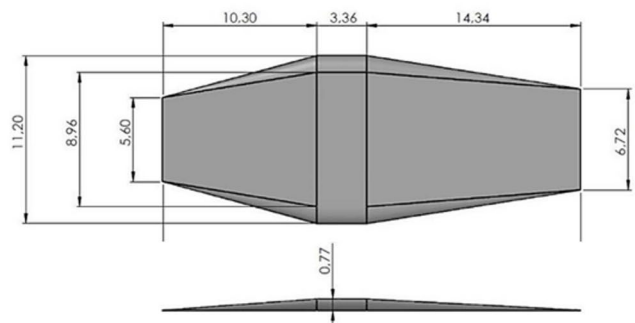


Fig. 2 On the left, the oil flow visualization of the OAT15A airfoil model is shown in the presence of SCBs. The green solid and dashed lines indicate the three PIV measurement planes. On the right, a



sketch of the SCB with dimensions is reported. Figures adapted from D'Aguanno et al. (2023)

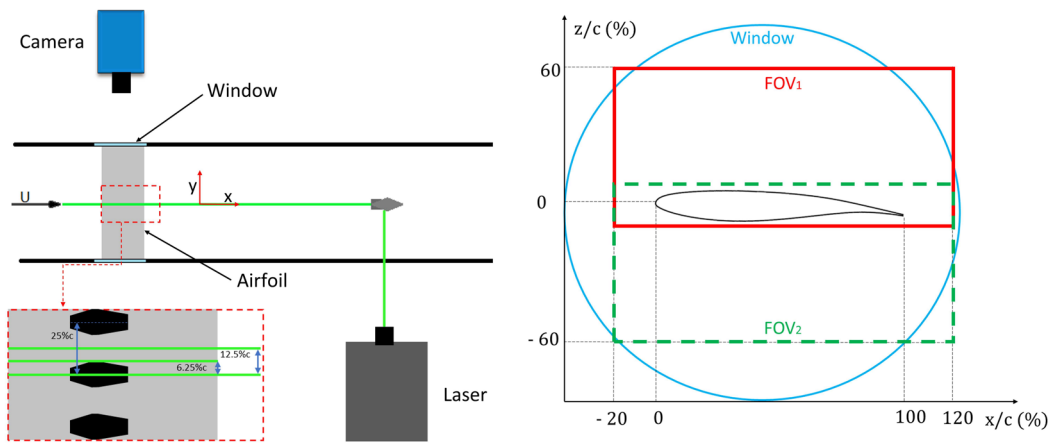


Fig. 3 Sketch of the PIV setup on the left. On the right, indication of the PIV FOV, on both the suction (FOV_1 , red) and pressure side (FOV_2 , green) of the airfoil

approximately 1 mm was generated. The current settings allowed the retrieval of velocity data around the entire airfoil apart from a small isentropic region at the leading edge, caused by the shadow created by the airfoil itself.

2.1.3 PIV processing and uncertainty

To reduce the effect of reflections of the laser on the airfoil and on the SCBs, a Butterworth filter was applied, using a filter length of seven images (Sciacchitano and Scarano (2014)). Thereafter, the cross-correlation was computed with a multi-pass approach, with one pass with a window size of $64 \text{ px} \times 64 \text{ px}$ ($2.5 \text{ mm} \times 2.5 \text{ mm}$) and an overlap of 50% and then two passes with a final window size of $32 \text{ px} \times 32 \text{ px}$ ($1.9 \text{ mm} \times 1.9 \text{ mm}$) and an overlap of 75%, resulting in a vector spacing of $0.44\%c$. The main PIV processing settings are summarized in Table 3.

The PIV measurements are affected by an experimental uncertainty, and here the main sources are briefly discussed. The first contribution is associated with the cross-correlation calculation (see Humble (2009) for more details) and is quantified as lower than 2 m/s in the entire FOV. The second contribution is associated with the particle slip effect (Ragni et al. (2011)) which is relevant only directly downstream of the shockwave ($\epsilon_{\text{slip}} = 40 - 60 \text{ m/s}$). Since time-averaged (and phase-averaged) velocity vectors will be discussed in this study, the statistical uncertainties of the two velocity components are here reported and are equal to $\epsilon_{\bar{u}} < 4.5 \text{ m/s}$ and $\epsilon_{\bar{v}} < 1.9 \text{ m/s}$. When analyzing the propagation of error from the velocity field to the pressure coefficient, it is possible to obtain that $\Delta C_p \approx -2 \frac{\Delta V}{V}$ (see van Oudheusden (2008)), meaning that for a relative error in the absolute

Table 3 PIV parameters and uncertainties

Parameter	Symbol	Value	Unit
Acquisition frequency	f	15	Hz
Pulse separation	dt	3	μs
Number of images	N	700	
Image resolution		2560×2160	px
Final window size	WS	32×32	px
Window overlap		75	%
Vector spacing		0.44	% c
Cross-correlation unc	ϵ_{cc}	< 1.8	m/s
Particle slip	ϵ_{slip}	40 – 60 (SW)	m/s
Statistical unc. u	$\epsilon_{\bar{u}}$	4.5	m/s
Statistical unc. v	$\epsilon_{\bar{v}}$	1.9	m/s
Uncertainty C_p	ϵ_{C_p}	0.02	
Uncertainty C_l	ϵ_{C_l}	0.04	
Uncertainty C_d	ϵ_{C_d}	0.004	

velocity in the order of 1% (as in this study), an uncertainty in pressure coefficient of about 0.02 is expected.

2.2 Pressure and load determination

In this study, the loads are not determined from an integration of the surface pressure distribution, since this procedure from PIV data is challenging (in view of, e.g., reflections and shadow effects), and in particular, the suction peak is commonly not accurately captured (see, e.g., Ragni et al. (2009); Tagliabue et al. (2017)). Furthermore, the frictional drag component is not included. This would make the determination of the aerodynamic loads from such a procedure highly unreliable. Instead, the loads are determined from an integral momentum balance (control volume) approach

(van Oudheusden et al. (2007)). This does not require to have pressure data at the airfoil surface itself, but only on an integration contour around the airfoil. This procedure requires as a first step the estimation of the pressure field. Sufficiently far away from the airfoil the flow can be considered inviscid and adiabatic; thus, the isentropic relations (in combination with the ideal gas law) can be used to obtain the temperature and the pressure:

$$\frac{T}{T_\infty} = 1 + \frac{\gamma - 1}{2} M_\infty^2 \left(1 - \frac{V^2}{V_\infty^2} \right) \tag{1}$$

$$\frac{p}{p_\infty} = \left(1 + \frac{\gamma - 1}{2} M_\infty^2 \left(1 - \frac{V^2}{V_\infty^2} \right) \right)^{\frac{\gamma}{\gamma - 1}} \tag{2}$$

These assumptions are not valid in the wake, where the flow is rotational. Using the assumption (as a first approximation) that viscous effects are only relevant in the region in close proximity to the airfoil surface and that the flow is steady, the differential form of the momentum equation allows the expression of the local pressure gradient, as:

$$-\frac{\nabla p}{\rho} = \frac{\rho}{p} (V \cdot \nabla) V \tag{3}$$

The term ρ/p can be derived from the steady, adiabatic energy equation (equivalent to a constant total temperature assumption) and from the ideal gas equation (van Oudheusden et al. (2007)), yielding:

$$\frac{\rho}{p} = \frac{\gamma M_\infty^2}{V_\infty^2 + \frac{\gamma - 1}{2} M_\infty^2 (V_\infty^2 - V^2)} \tag{4}$$

Thus, an equation that relates the pressure field to the velocity field is obtained:

$$\frac{\nabla p}{p} = \nabla \ln(p) = - \frac{\gamma M_\infty^2}{V_\infty^2 + \frac{\gamma - 1}{2} M_\infty^2 (V_\infty^2 - V^2)} (V \cdot \nabla) V \tag{5}$$

A space marching algorithm is subsequently used to extract the pressure from Eq. 5, using the isentropic pressure as initial conditions in the freestream, similarly to van Oudheusden (2008). The pressure field is thus obtained by a spatial integration, using at each step all the immediate neighbors in which the pressure is known or computed as in Baur and Kongeter (1999).

Assuming a two-dimensional and statistically steady flow, the resultant aerodynamic force (R) on the airfoil can be evaluated by using the Reynolds-averaged momentum equation in its integral form on a contour integral around the airfoil (see Anderson (2011)). Following the same procedure as in Ragni et al. (2009), the freestream momentum is subtracted to reduce uncertainties.

$$R = - \iint \rho (V \cdot n) (V - V_\infty) dS + \iint (-pn + \bar{\tau} \cdot n) dS \tag{6}$$

From R , both lift and drag components can be derived using a Cartesian frame of reference. The integration contour used for the evaluation of the lift coefficient is reported in Fig. 4.

Evaluating the flow quantities around the entire contour can result in accumulation of uncertainty, which could lead to an inaccurate estimation of the loads, in particular for the drag (van Oudheusden et al. (2006)). It is worth mentioning that for most of the flow domain the pressure is not determined by spatial integration but relies instead on the isentropic relations, which is reasonably justified for the current conditions within measurement uncertainty (Ragni et al. (2009)). Spatial integration is only applied in the wake region, using the isentropic pressure in the outer flow as boundary conditions. This procedure strongly mitigates the effects of integration error propagation and the boundary conditions. Also, it does not require any regions with free

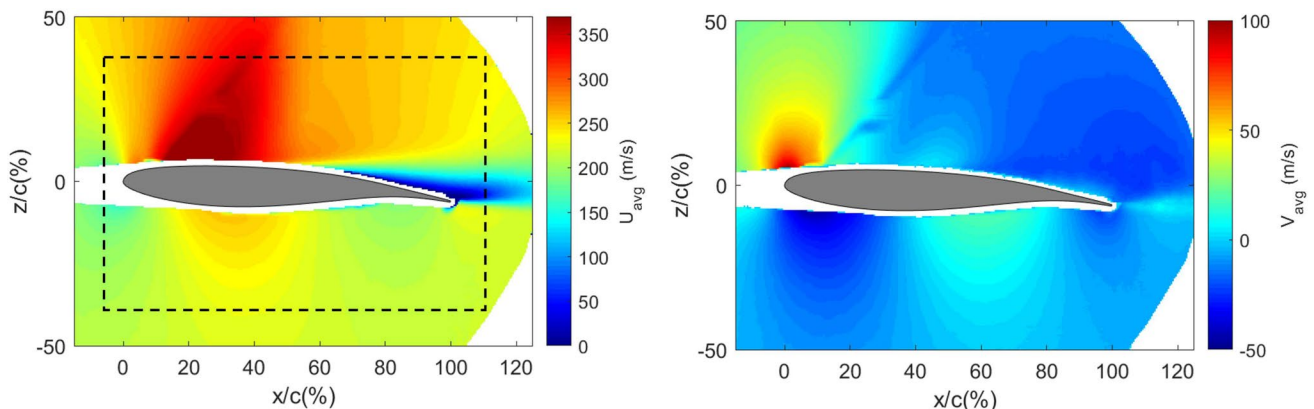


Fig. 4 Average horizontal (left) and vertical (right) velocity field for the clean configuration

stream flow conditions, with only the knowledge of the reservoir conditions sufficient.

However, in view of higher uncertainties deriving from a contour integral procedure, the drag is evaluated from the momentum deficit in the wake, based on the same approach proposed by Jones (1936). Following Ragni et al. (2009), it is assumed that at a certain location (“1”) sufficiently downstream of the airfoil, the pressure has recovered the freestream value $p_1 = p_\infty$. However, in view of the limited optical access in the wind tunnel, this location is not available and, instead, the pressure is reconstructed up to a location (“2”) where the pressure has not reached the freestream value yet. However, by using momentum balance, conservation of mass and taking into account compressibility effects, the following expression for the drag coefficient (C_d) is derived (Ragni et al. (2009)):

$$C_d = 2 \int_{z_A/c}^{z_B/c} \left(\frac{p_2}{p_\infty} \right)^{\frac{1}{\gamma}} \left(\frac{p_{02}}{p_{0\infty}} \right)^{\frac{\gamma-1}{\gamma}} \sqrt{\frac{1 - \left(\frac{p_2}{p_{02}} \right)^{\frac{\gamma-1}{\gamma}}}{1 - \left(\frac{p_\infty}{p_{0\infty}} \right)^{\frac{\gamma-1}{\gamma}}}} \left[1 - \sqrt{\frac{1 - \left(\frac{p_\infty}{p_{02}} \right)^{\frac{\gamma-1}{\gamma}}}{1 - \left(\frac{p_\infty}{p_{0\infty}} \right)^{\frac{\gamma-1}{\gamma}}}} \right] d(z/c) \tag{7}$$

where the subscript “0” indicates total conditions, while z_A and z_B indicate respectively the vertical location of the bottom and the top of the integration domain.

On the one hand, since near the airfoil the error in the computation of lift is larger in view of higher velocity gradients, the lift coefficient will always be estimated for the same contour as far away as possible from the airfoil, as shown in Fig. 4. On the other hand, for the drag coefficient evaluation, the drop in total pressure has been evaluated at $x_2/c = 120\%$.

The pressure and load reconstruction procedure was verified using data from a supporting RANS simulation under conditions similar to those of the experiments. These data were used to validate the lift and drag estimation procedures by comparing direct numerical pressure data with those derived from numerical velocity fields. Additionally, the numerical dataset was used to guide the selection of PIV spatial resolution and to determine the optimal streamwise location of plane 2 for drag estimation. However, this numerical dataset is not intended to provide further insight into the buffet phenomenon. Given the scope of this study and to maintain focus, these data have not been included in the paper. Furthermore, this particular procedure for deriving the 2D airfoil loads from PIV data (i.e., lift from a contour integral and drag from a wake integral) has been previously tested in both low-speed (van Oudheusden et al. (2006)) and transonic (Ragni et al. (2009)) studies. In both cases the load results were validated against pressure tap data (for the lift) and a pitot-tube wake rake (for the drag). The current study directly follows the methodology as well as the measurement uncertainty assessment of the transonic airfoil study of Ragni et al. (2009), which was performed in the same wind tunnel and at similar flow conditions. As such we consider the methodology reliable and validated.

The measurement uncertainties for the load coefficients can be calculated by linearly propagating the uncertainties in the velocity and pressure coefficients. In the study by Ragni et al. (2009), where similar uncertainties in the pressure coefficient and velocity were reported, this analysis yielded an uncertainty of 0.04 for the lift coefficient and 0.004 for the drag coefficient. For reference, see also Table 3.

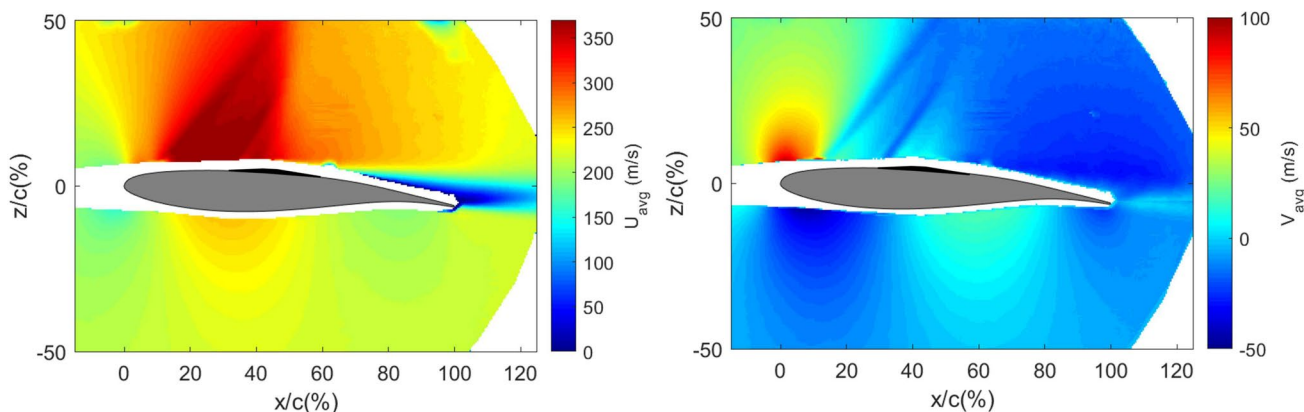


Fig. 5 Average horizontal (left) and vertical (right) velocity field for the SCB configuration ($y/c = 0\%$)

3 Results

3.1 Average flow field

The average velocity field around the entire airfoil is shown in Fig. 4 for the clean configuration and in Fig. 5 for the SCB configuration ($y/c = 0\%$) for both the horizontal (left) and the vertical (right) velocity components. The average streamwise velocity field for the SCB case highlights the presence of an oblique shockwave that emanates from the leading edge of the SCB and a quasi-normal shockwave located at its crest. A slight reduction of the separated area region (taking the blue region as a proxy) is also observed for the controlled case. The comparison of the vertical average velocity fields reveals differences in correspondence of the shock control bump, with an increase in vertical velocity induced by the front part of the bump ($35 < x/c < 45\%$). Two oblique lines are observed for the SCB configuration (only one for the clean case), in correspondence of the transition trip and of the oblique shockwave. These lines are associated with optical aberration effects, which are well known to affect planar PIV data (see Elsinga et al. (2005)) in particular, in locations where spanwise invariant density gradients are integrated. For both the vertical and the streamwise velocity component, no significant difference is observed on the pressure side of the airfoil, suggesting that geometry variations on the suction side of the airfoil have little or no effect on the pressure side velocity field.

To quantitatively compare the average flow field for all the measurements, in Fig. 6 streamwise velocity profiles are shown at 60, 75, 90, 105 and 120% c for the clean and all the SCB measurement planes ($y/c = 0; 6.25$ and 12.5%). Apart from a region very close to the surface of the airfoil, the SCB centerline configuration ($y/c = 0\%$) always displays

an increase in velocity compared to the clean configuration and similar results are obtained for $y/c = 6.25\%$. Part of this velocity increase is due to reduced losses through the shockwave structures in the presence of SCBs; this is particularly evident for $x/c = 60\%$, which is a location just downstream of the shockwave oscillation range. Differently, for lower values of "z", the increase in velocity in the presence of SCBs is associated with a reduction of the extent of the shear layer and separated area. This is also evident in the wake of the airfoil ($x/c = 105\%; x/c = 120\%$), where a "fuller" velocity profile is observed for the clean configuration. A completely different behavior is observed in the symmetry plane between adjacent SCBs ($y/c = 12.5\%$) for which lower values of the streamwise velocity component are observed close to the surface of the airfoil, suggesting an increase in separated area size at this location. However, for $z/c > 10\%$, values of velocity similar to the other SCB measurement planes are obtained, suggesting that at this location, the effect of the spanwise position is not relevant anymore. It should also be taken into account that these velocity profiles lack information in close proximity to the airfoil surface, due to laser reflections.

3.2 Shockwave position

From the velocity fields the shockwave position has been tracked by means of the horizontal velocity gradient at z/c

Table 4 Shockwave statistics

	Clean	SCB ($y/c = 0\%$)	SCB ($y/c = 6.25\%$)	SCB ($y/c = 12.5\%$)
$X_{SW\ AVG}$ (% c)	43.0	46.9	48.4	49.7
$X_{SW\ STD}$ (% c)	6.4	4.2	3.7	3.5

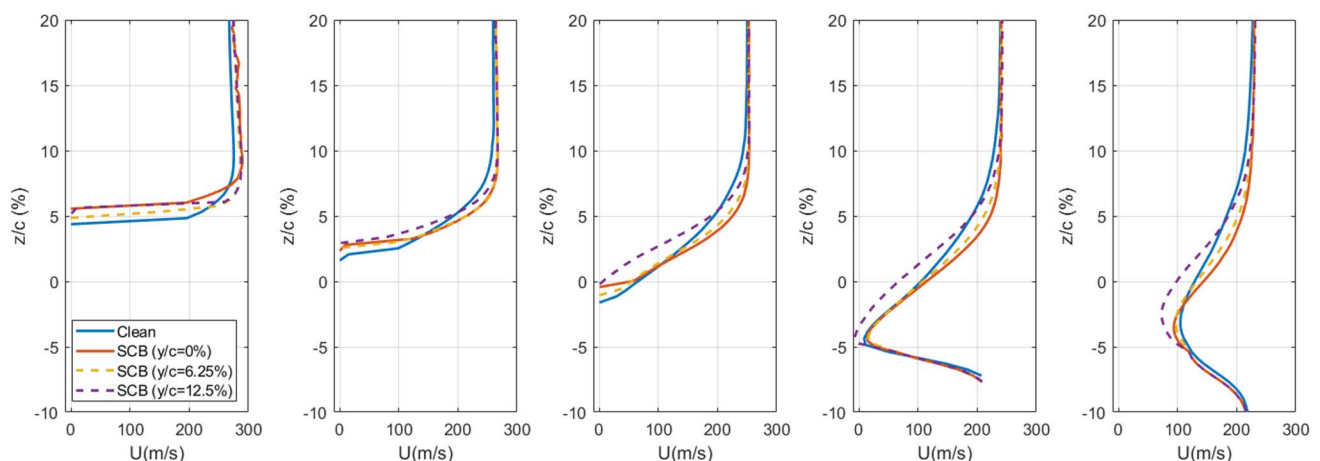


Fig. 6 Profiles of streamwise velocity component for clean and SCB configurations for five chordwise locations (from left to right): $x/c = 60\%; 75\%; 90\%; 105\%; 120\%$

= 10% for both the clean and the SCB case. The values of the average ($X_{SW\ AVG}$) and the standard deviation ($X_{SW\ STD}$) of the shock position are reported in Table 4. By comparing the SCB performance at different measurement planes, it is clarified that the average shockwave position is located more downstream for the off-center measurement planes in view of the curvature in the spanwise direction of the oblique shockwave. The standard deviation of the shockwave position, instead, clearly indicates that in the presence of SCBs the amplitude of the shockwave oscillation is reduced, with values close to the ones reported in D’Aguanno et al. (2023).

To better visualize the reduction in extent of the shockwave oscillation range, the probability density function of the shock location is reported in Fig. 7. The shockwave oscillation range is evidently smaller with SCBs compared to the clean case (with a reduction of the range of about 30%). Among the three spanwise SCB measurement locations, the range of oscillation of the shockwave

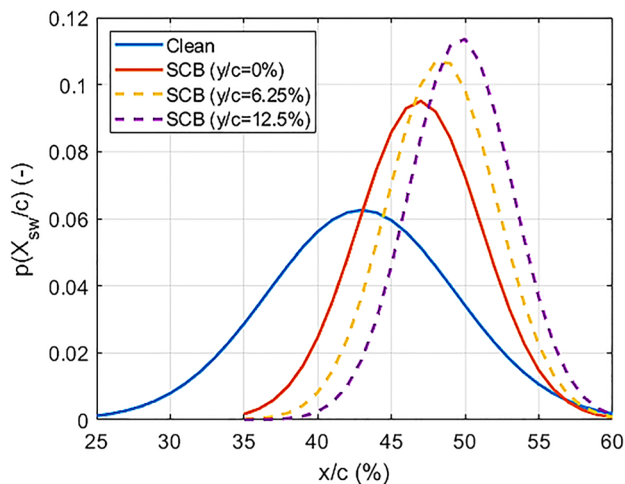
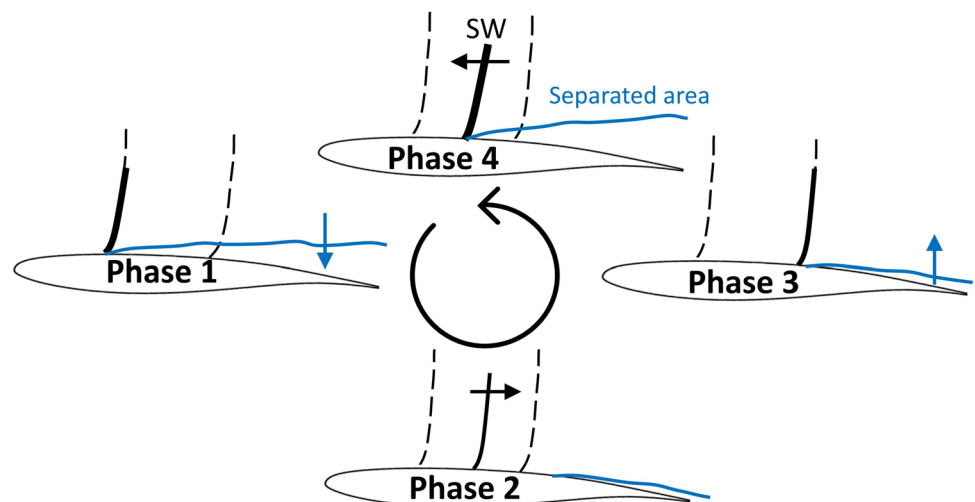


Fig. 7 Pdf of shock position for clean and SCB configurations

Fig. 8 Sketch of shockwave position and separated area extent in four buffet phases



is clearly wider for $y/c = 0\%$, while it is decreased at more off-center locations. Furthermore, the shockwave appears located much more upstream at the centerline. These observations are in agreement with the shockwave position statistics reported in Table 4. It is also interesting to note that for the controlled case, in view of the presence of the SCBs, the most downstream shockwave location is not significantly affected, while the most upstream position is located $10\%c$ more downstream than for the clean case.

3.3 Phase average definition

By virtue of the known periodicity of the transonic buffet phenomenon (see Giannelis et al. (2017); Jacquin et al. (2009); D’Aguanno et al. (2021a)), from the instantaneous PIV images the phase-averaged velocity fields are obtained. In total four buffet phases have been defined for this study: with the shockwave in its most upstream position (1), during its downstream movement (2), with the shockwave in its most downstream position (3) and with the shockwave moving upstream (4). A sketch of the separated area extent and the shockwave position for each phase is given in Fig. 8.

Since the shock position is not time resolved, the different phases are not defined according to the shockwave velocity but according to the shock position and the extent of the separated area. The shock position value distinguishes only phase 1 and 3, while the extent of the separated area allows to discern between phase 2 and 4. This phase definition is based on the results of Grossi et al. (2014) and D’Aguanno et al. (2021a), which clearly showed that the separated area is correlated with the shockwave position and direction and has its widest extent during its upstream movement and the smallest during the downstream travel. The number of snapshots used to compute the phase-averaged statistics is indicated in

Table 5 Number of snapshots per buffet phase

	Clean	SCB ($y/c = 0\%$)	SCB ($y/c = 6.25\%$)	SCB ($y/c = 12.5\%$)
Phase 1	177	189	148	172
Phase 2	208	178	231	209
Phase 3	177	173	195	160
Phase 4	138	160	126	159

Table 5 for each phase and for all the measurement cases. The highest and lowest number of snapshots, respectively, in phase 2 and 4 confirms the observation of D'Aguzzo et al. (2021a), which showed that the shockwave has the highest absolute velocity when moving upstream and the lowest during its downstream travel.

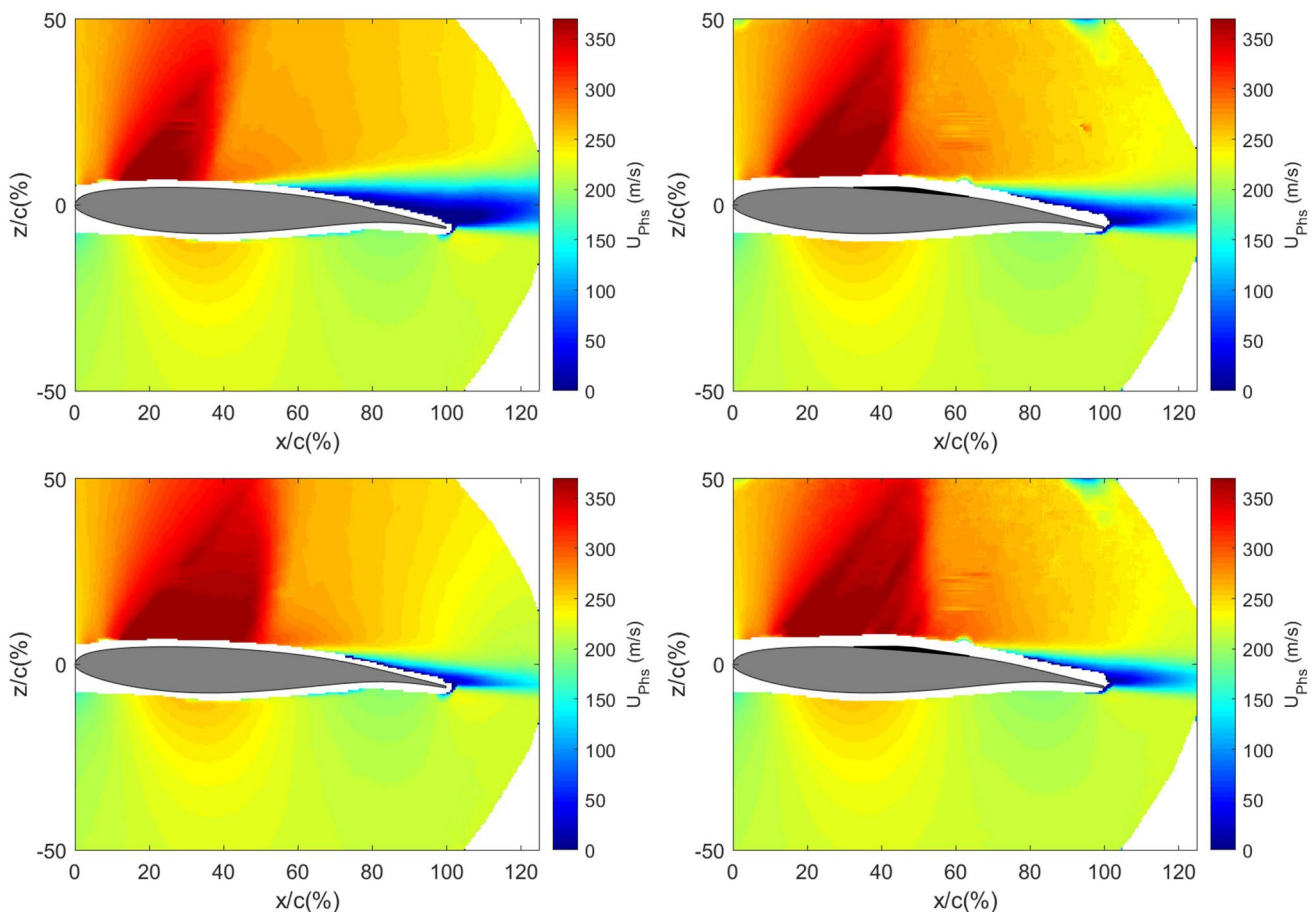
Once the four phases are defined, the phase-averaged velocity fields are obtained by computing the mean of all the snapshots belonging to each phase. Assuming a triple decomposition of the velocity field, as:

$$\vec{u} = \vec{u}_{\text{avg}} + \vec{u}_{\text{per}} + \vec{u}_{\text{turb}} \quad (8)$$

the phase-averaged velocity field is given by the sum $\vec{u}_{\text{per}} + \vec{u}_{\text{avg}} = \vec{u}_{\text{phs}}$ (periodic and average contribution) and is plotted in Fig 9 for both the clean (left) and the SCB ($y/c = 0\%$) (right) configurations in the most upstream (top) and downstream (bottom) shockwave position. The first relevant difference is about the shockwave excursion between these two phases, which for the SCB case is much more limited with the quasi-normal shockwave ranging between the SCB crest and just 5% downstream of it. Similarly, while for the clean case the separated area undergoes a wide variation in its size between phase 1 (small) and phase 3 (large), for the SCB configuration there are minor variations in separated area extent between these two phases. This observation confirms the stabilizing effect associated with the presence of SCBs.

3.4 Pressure estimation

With the assumption of an adiabatic and inviscid flow, the pressure field is obtained using the isentropic relation

**Fig. 9** Phase-averaged velocity fields for clean (left) and SCB $y/c = 0\%$ (right) configurations in phase 1 (top) and 3 (bottom)

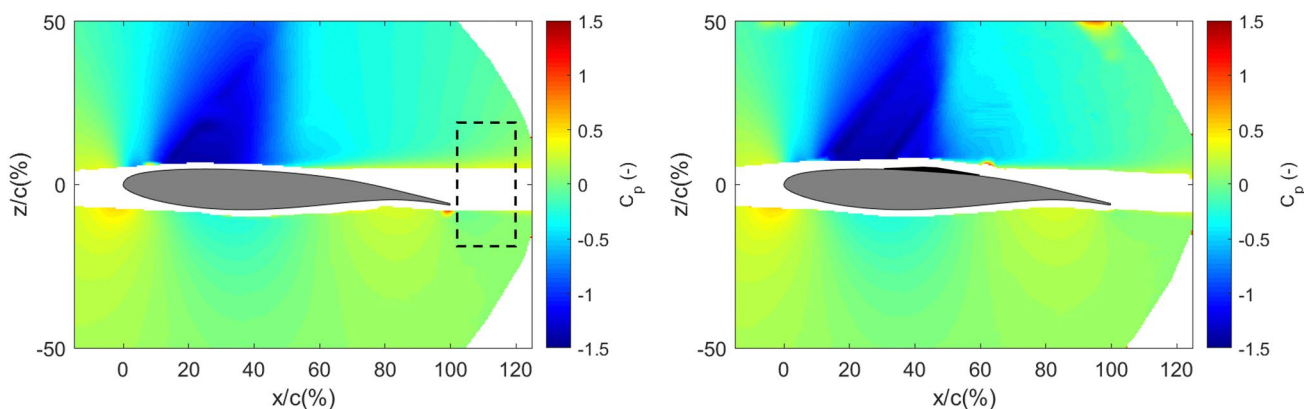


Fig. 10 Isentropic static pressure field for clean (left) and SCB $y/c = 0%$ (right) configurations

(Eq. 2), see Fig. 10 for the clean and the SCB ($y/c = 0%$) configurations. By comparing the two pressure fields, it is observed that for the SCB case the low-pressure area associated with the supersonic region is wider and more intense with respect to the clean case. This is in agreement with the more downstream average shockwave position. Additionally, downstream of the average shockwave position ($45 < x/c < 65%$) a wider region of low static pressure is observed for the SCB case for $0 < z/c < 25%$ (below the triple point of the λ -shockwave structure). This beneficial effect could be linked with the less dissipative compression which is taking place across the two lower legs of the λ -shockwave compared to the quasi-normal shockwave case for the clean airfoil. Although this model predicts relatively high-pressure values in the wake (region which for this reason has been masked in Fig. 10), it brings to reliable

lift estimations, as for the study of Ragni et al. (2009) on a NACA 0012 airfoil.

However, as previously commented, the isentropic pressure distribution cannot be used to accurately compute the drag coefficient since it yields incorrect values in the wake area, where the flow is clearly rotational. In this region (delimited by the black dashed contour in Fig. 10, left), the static pressure field has been obtained using Eq. 5 (see Fig. 11, left). The pressure field derived from the rotational formulation is here shown only for the clean configuration, with qualitatively similar distributions occurring for the different SCB measurement planes. To better quantify differences among the tested configurations, Fig. 11 (right) shows the profile of the total pressure p_0 (relative to the freestream total pressure, $p_{0,\infty}$) in the wake area, reported along the vertical direction ($-20 < z/c < 20%$). The figure shows similar results for $-20 < z/c < -5%$ (pressure side), confirming the

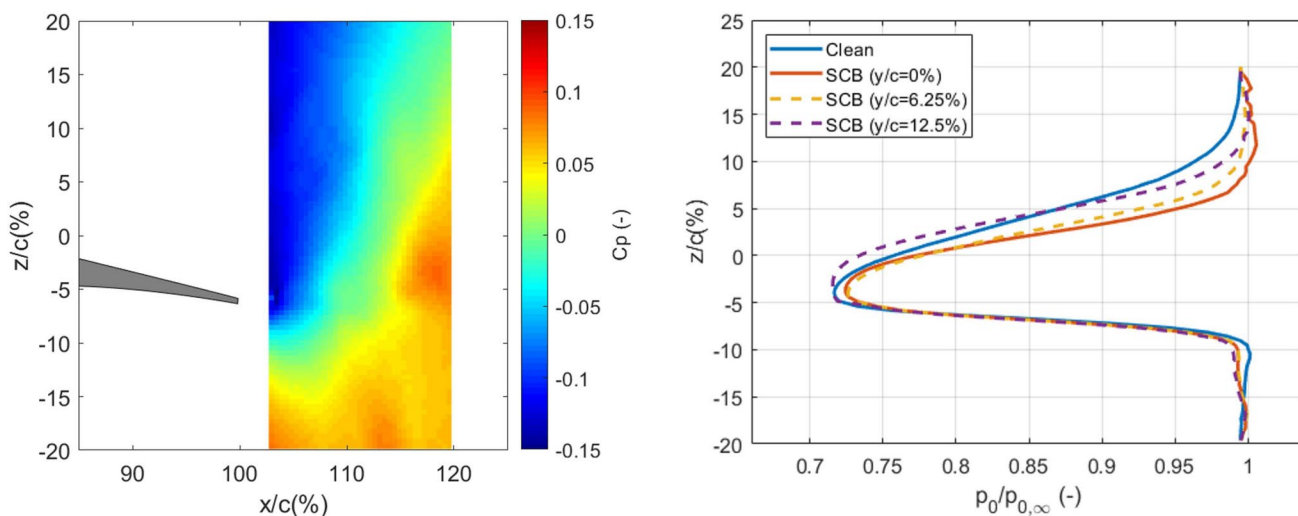


Fig. 11 Rotational pressure coefficient field for clean airfoil (left). On the right, comparison of relative total pressure profile for $x/c = 120%$, for clean and SCB configurations

reduced influence of SCBs on the pressure side. However, important differences are observed for $-5 < z/c < 20\%$, with the SCB configurations at $y/c = 0\%$ and $y/c = 6.25\%$ clearly having lower total pressure losses when compared to the clean model. Minor differences are instead observed between the clean and the SCB cases in the most outboard measurement plane ($y/c = 12.5\%$).

It should be noted that, although the steady assumption used for obtaining Eq. 3 is generally not applicable to transonic buffet flow, the flow can be considered quasi-steady for each buffet phase. While the phase-averaged pressure fields are not directly shown here, the corresponding phase-averaged loads will be discussed in the following section.

3.5 Lift and drag evaluation

From the pressure fields, the lift (C_l) and drag (C_d) coefficients are obtained, respectively, from Eq. 6 and Eq. 7 for both the clean and the shock control bump configurations. The average value of the lift coefficient (reported in Table 6) is evidently increased for the controlled configuration in all the measurement planes. An opposite trend is present for the drag coefficient, with C_d being slightly increased only for $y/c = 12.5\%$ in the presence of SCBs. This behavior suggests that the use of SCBs not only decreases the buffet shockwave

and separated area oscillations, but it has also beneficial effects on the loads experienced by the airfoil. This is associated with an extension of the supersonic area and a decrease of the extent of the separated area for the SCB case.

From the phase-averaged velocity data, C_l and C_d were computed for each buffet phase separately for both the clean and the SCB configuration. In this study the global loads in the presence of SCBs are approximated by the average of the loads at the three equally spaced measurement planes ($y/c = 0; 6.25, 12.5\%$). Although this is an approximation, it gives a better overall estimation of the lift and drag values than simply considering one spanwise location.

The phase-averaged values of the coefficients (see Fig. 12) confirm that, not only the average value of the lift and the drag coefficients are, respectively, slightly increased and reduced in the presence of SCBs, but also their amplitude of oscillation is diminished. This is also well described by the values of ΔC_l and ΔC_d (reported in Table 6), which are defined as the difference between the highest and the lowest values of these coefficients in the four buffet phases. The data show a reduction of the oscillation of the phase-averaged values in the presence of SCBs of approximately 70% for the lift coefficient and 40% for the drag coefficient.

In terms of phase-averaged values, the highest values for C_l are always achieved in phase 3, while the lowest in phase

Table 6 Lift and drag values

	Clean	SCB ($y/c = 0\%$)	SCB ($y/c = 6.25\%$)	SCB ($y/c = 12.5\%$)
C_l (average)	0.81	0.84	0.83	0.83
C_d (average)	0.058	0.048	0.054	0.060
$\Delta C_l = (C_{l,Phs})_{max} - (C_{l,Phs})_{min}$	0.14	0.05	0.06	0.06
$\Delta C_d = (C_{d,Phs})_{max} - (C_{d,Phs})_{min}$	0.032	0.020	0.020	0.014

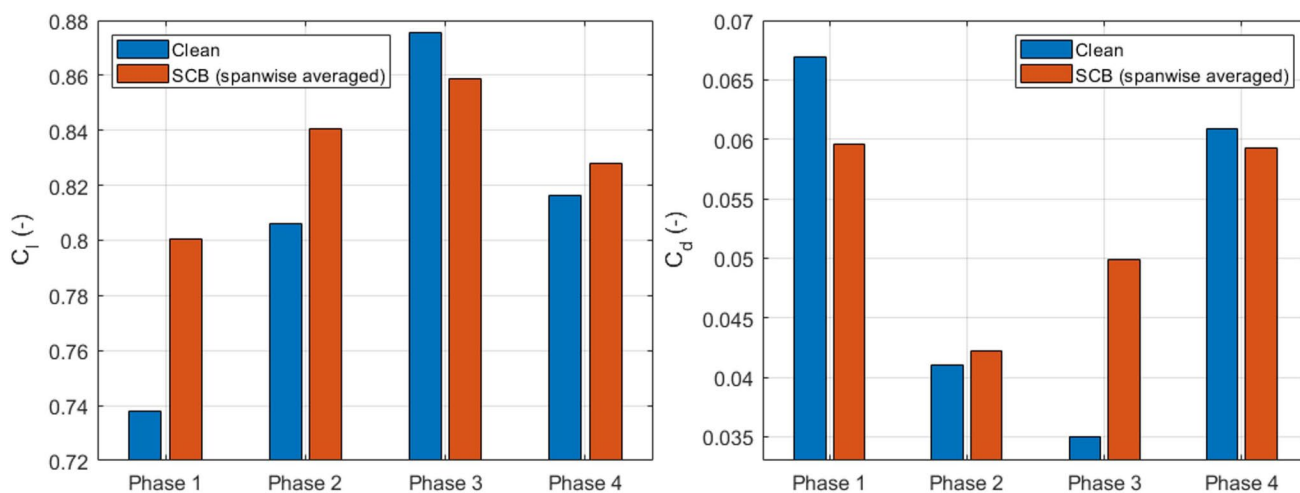


Fig. 12 Lift (left) and drag (right) coefficients for the clean and the SCB configurations. The SCB data are here obtained by averaging the results in the three measurement planes ($y/c = 0; 6.25; 12.5\%$)

1. This behavior is expected and mainly associated with the supersonic area extending over a wider region in phase 3 (shockwave in its most downstream position). It is worth mentioning that phase 3 is the only phase in which the lift has a higher value for the clean configuration with respect to the SCB case. This behavior is associated with the shockwave being located more downstream for the clean case and therefore having a larger supersonic area, an opposite trend is present in phase 1.

Regarding the drag coefficient (C_d), the most significant differences between the clean and SCB configurations are observed in phase 3 (higher C_d for the SCB case) and phase 1 (higher C_d for the clean case). Conversely, the highest C_d values overall are found in phases 1 and 4, corresponding to the largest extent of the separated area. For these phases, the lower C_d values in the SCB case are attributed to an overall reduction in the extent of the wake area.

To better understand the behavior of the SCB configuration, the effect of the spanwise location is addressed in Fig. 13 where the phase-averaged values of the aerodynamic coefficients are reported for the three measurement planes. The plot highlights significant differences of the values of the coefficients at these spanwise locations, in particular for C_d . This behavior can be ascribed to the large variability of the extent of the wake in the three planes, which is confirmed by the total pressure profile in Fig. 11 (right) and the streamwise velocity profiles in Fig. 6. For $y/c = 0\%$ the streamwise vortices that are generated at the sides of the SCBs (see Ogawa et al. (2008)) are considered to be responsible for a consistent reduction of the extent of the separated area, while this effect is less relevant at more outboard locations, yielding to higher values of C_d . From the SCBs data at different measurement planes, it can be concluded that the increase in drag in phase 3 for the

SCB case with respect to the uncontrolled configuration is mainly associated with the $y/c = 12.5\%$ measurement plane. This large variation in drag coefficient between the different measurement planes confirms that the spacing of the SCBs is an important parameter for drag alleviation purposes.

For the lift coefficient, minor differences are present among the different measurements planes, with a slightly higher (average) lift coefficient value obtained for $y/c = 0\%$ (see also Table 6). Furthermore, the trend of the phase-averaged values is consistent in the different measurement planes, with the highest values for C_l always achieved in phase 3, while the lowest in phase 1.

4 Discussion and conclusions

This study shows that properly designed and spaced shock control bumps can reduce the shockwave and aerodynamic coefficients fluctuations under fully developed buffet conditions. The velocity data have highlighted the main flow features associated with the presence of SCBs, including the λ -shockwave and a reduced separated area. The presence of SCBs resulted in a reduction of the shockwave oscillation range and of the standard deviation of the shockwave position of about 30%.

The quantification of the aerodynamic loads around the airfoil showed a 17% decrease of C_d and roughly a 4% increase of C_l in the presence of SCBs; thus, these variations resulted in a 25% increase of L/D . It should be noted that this value is well above the increase reported in the literature for steady impinging shockwave applications (see for example Eastwood and Jarrett (2012), where a 10% increase of L/D reported). This improvement is not surprising in view of the optimized spacing of the SCBs and

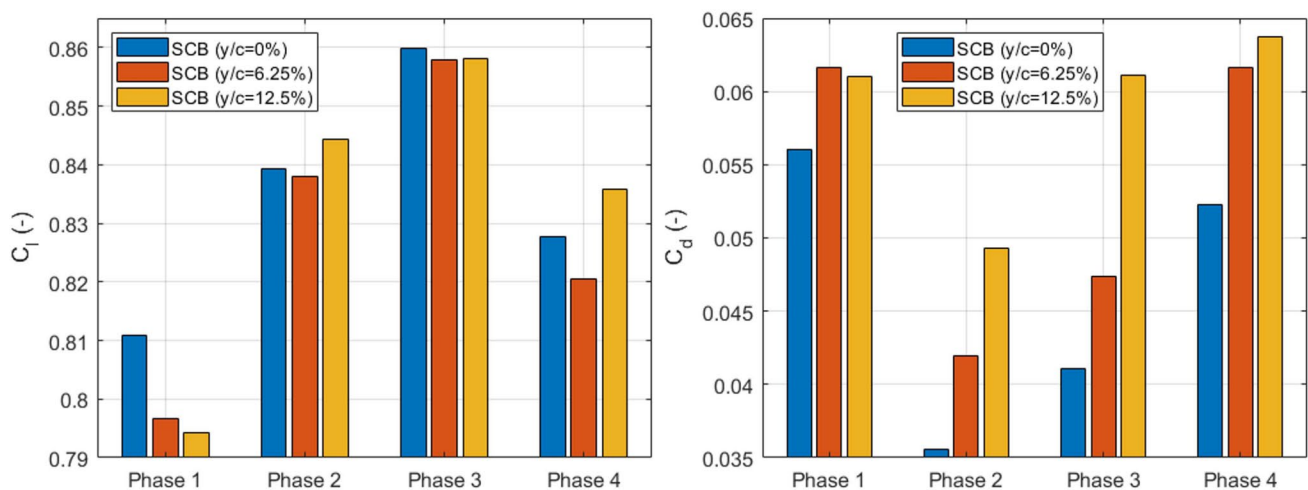


Fig. 13 Lift (left) and drag (right) coefficients values for different SCB measurement planes and for the four buffet phases

the double working principle of SCBs for transonic buffet applications, which at the same time stabilize the shock position (reducing the occurrence of shockfoot separation) and promote attached flow thanks to the streamwise vortex development from the tail of the SCBs. The stabilization of the shock position even resulted in the extension of the supersonic area, which has direct positive consequences on the lift coefficient value. In addition to the streamwise vortex production, the reduction of C_d is mainly associated with a decrease of the extent of the separated area which could be linked to the lower velocity of the shockwave in the presence of SCBs. In fact, being the frequency of oscillation of the shockwave unchanged in the presence of SCBs (160 Hz, see D'Aguanno et al. (2023)) but the range of oscillation reduced, a lower shockwave velocity is obtained as a consequence. This aspect is particularly relevant in the upstream phase of the shock travel where a higher upstream shockwave velocity results in a stronger shockwave and thus causes a larger shockfoot separated area.

To evaluate the effect of SCBs on the different buffet stages, phase averaging was used, successfully implementing a new approach for determining the phases. This method is a single-snapshot approach which is only based on the values of the shock position and the extent of the separated area at a given time step and therefore, does not require to time-resolve the shockwave position. This approach is suggested for future applications where low-speed acquisition PIV systems are to be preferred, as for example when high spatial resolution data are required. The phase-averaged values of the aerodynamic coefficients have demonstrated that not only do SCBs avoid detrimental effects on the mean aerodynamic loads (a topic already investigated in other studies), but their implementation also results in a 70% reduction of the amplitude of oscillation for the lift coefficient and 40% reduction for C_d . This aspect is the most relevant, because of the direct positive influence it has on the fatigue life of an aerodynamic-structure undergoing transonic buffet.

The estimation of the aerodynamic loads at different measurement planes has shown non-negligible differences (in particular for the drag coefficient), with the best performance (highest lift and lowest drag) achieved in the symmetry plane of a SCB and the worst in the symmetry plane between adjacent bumps. This observation confirms that the characterization of a similar three-dimensional device cannot be evaluated at one specific spanwise location, like is often the case for pressure transducer measurements. By considering this variation, it is assumed that the overall aerodynamic coefficients of an airfoil in the presence of 3D SCBs can be obtained as the average of three properly spaced measurement planes.

This study demonstrates that PIV load estimation for transonic buffet applications is feasible and allows

the complete characterization of the flow field (both time-averaged and phase-averaged) around the airfoil. The combination of pressure gradient integration in the rotational area and isentropic pressure computation in the remaining FOV, in conjunction with planar PIV data is an attractive approach which could also be used in industrial applications. Although the results of this study have not been independently validated, such as with local pressure or force balance measurements, the load estimation methodology follows the approach proposed by Ragni et al. (2009) that was previously validated in the same wind tunnel on a similar flow case. This supports the confidence in the method as applied in the present work and as such the reliability of the current data. For future research studies, more complicated PIV setups could be used to estimate pressure in instantaneous snapshot and/or evaluating the variation of aerodynamic coefficients along the entire span (tomographic PIV).

3D SCBs are more versatile compared to 2D SCBs, and the results of this study demonstrate that properly spaced SCBs can outperform other configurations proposed in the literature in terms of lift coefficient under transonic buffet conditions. While 3D SCBs are also expected to perform better in off-design conditions, to mitigate any potential negative effects, an adaptive implementation of SCBs could be considered. In similar applications the use of wedge SCBs could be unfeasible and therefore, the use of rounded SCBs is suggested. A similar device has already proved to be effective in reducing the buffet loads in the numerical study of Geoghegan et al. (2020).

Author Contributions All authors contributed to the study conception, design and preparation. Data collection and analysis were performed by AD and AC. The first draft of the manuscript was written by AD. AD, FS, and BvO commented on previous versions of the manuscript. All authors read and approved the final manuscript.

Funding This work has been carried out as part of the project HOMER (Holistic Optical Metrology for Aero-Elastic Research), funded by the European Commission, program H2020 under Grant No. 769237.

Data Availability Data and materials that support the findings of this study are available on request from the corresponding author.

Declarations

Conflict of interest The authors declare they have no conflict of interest.

Ethical Approval Not applicable.

Open Access This article is licensed under a Creative Commons Attribution 4.0 International License, which permits use, sharing, adaptation, distribution and reproduction in any medium or format, as long as you give appropriate credit to the original author(s) and the source, provide a link to the Creative Commons licence, and indicate if changes

were made. The images or other third party material in this article are included in the article's Creative Commons licence, unless indicated otherwise in a credit line to the material. If material is not included in the article's Creative Commons licence and your intended use is not permitted by statutory regulation or exceeds the permitted use, you will need to obtain permission directly from the copyright holder. To view a copy of this licence, visit <http://creativecommons.org/licenses/by/4.0/>.

References

- Accorinti A, Baur T, Scharnowski S, Kähler CJ (2022) Experimental investigation of transonic shock buffet on an OAT15A profile. *AIAA J* 60:6289–6300
- Anderson J (2011) *Fundamentals of Aerodynamics*. McGraw Hill, 5th edition
- Babinsky H, Ogawa H (2008) SBLI control for wings and inlets. *Shock Waves* 18:89–96
- Bannink WJ, Bakker P (1983) Transonic mach number determination in a blow-down tunnel with solid walls and a downstream throat
- Baur T, Kongeter J (1999) PIV with high temporal resolution for the determination of local pressure reductions from coherent turbulent phenomena. In: 3rd Int Workshop on PIV, 16-18 September, Santa Barbara, California. Santa Barbara
- Bogdanski S, Nubler K, Lutz T, Kramer E (2014) Numerical investigation of the influence of shock control bumps on the buffet characteristics of a transonic airfoil. In: *New Results in Numerical and Experimental Fluid Mechanics IX*. p. 23–32
- Brion V, Dandois J, Mayer R, Reijasse P, Lutz T, Jacquin L (2019) Laminar buffet and flow control. *Proceed Institution Mech Eng Part G J Aero Eng* 234(1):124–139
- Bruce PJK, Babinsky H (2012) Experimental study into the flow physics of three-dimensional shock control bumps. *J Aircraft* 49:1222–1233
- Bruce PJK, Colliss SP (2015) Review of research into shock control bumps. *Shock Waves* 25:451–471
- Caruana D, Mignosi ACR, Corregge M (2003) Active control of transonic buffet flow. *Flow Turbulence Combustion* 824:312–351
- Caruana D, Mignosi A, Robitaille C, Corregge M (2003) Separated flow and buffeting control. *Flow Turbulence Combustion* 71:221–245
- Colliss SP, Babinsky H, Nubler K, Lutz T (2016) Vortical structures on three-dimensional shock control bumps. *AIAA J* 54:2338–2350
- Crouch J, Garbaruk A, Magidov D (2007) Predicting the onset of flow unsteadiness based on global instability. *J Comput Phys* 224:924–940
- Crouch J, Garbaruk A, Strelets M (2019) Global instability in the onset of transonic-wing buffet. *J Fluid Mech* 881:3–22
- D'Aguanno A, Schrijer FFJ, van Oudheusden BW (2021) Experimental investigation of the transonic buffet cycle on a supercritical airfoil. *Experiments Fluids* 62:214
- D'Aguanno A, Schrijer FFJ, van Oudheusden BW (2021) Spanwise organization of upstream traveling waves in transonic buffet. *Phys Fluids* 33:106105
- D'Aguanno A, Schrijer FFJ, van Oudheusden BW (2022) Experimental characterization of upper trailing edge flaps for transonic buffet control. *Flow Turbulence Combustion* 110(2):325–350
- D'Aguanno A, Schrijer FFJ, van Oudheusden BW (2023) Investigation of three-dimensional shock control bumps for transonic buffet alleviation. *AIAA J* 61:3419–3431
- Despre C, Caruana D, Mignosi A, Reberga O, Corregge M (2001) Buffet active control - experimental and numerical results. In: *Proceed RTO AVT Symposium Active Control Technol Enhanced Perform Operation Capabilities Military Aircraft, Land Vehicles, and Sea Vehicles*, June, Germany
- Eastwood JP, Jarrett JP (2012) Toward designing with three-dimensional bumps for lift/drag improvement and buffet alleviation. *AIAA J* 50:2882–2898
- Elsinga GE, van Oudheusden BW, Scarano F (2005) Evaluation of aero-optical distortion effects in PIV. *Experiments Fluids* 39:246–256
- Feldhusen-Hoffmann A, Lagemann C, Loosen S, Meysonnat P, Klaas M, Schröder W (2021) Analysis of transonic buffet using dynamic mode decomposition. *Experiments Fluids* 62:66
- Garnier E, Deck S (2010) Large-eddy simulation of transonic buffet over a supercritical airfoil. In: Armenio V, Geurts B, Fröhlich J (eds) *Direct and Large-Eddy Simulation VII*. Springer, Netherlands, Dordrecht, pp 549–554
- Geoghegan JA, Giannelis NF, Vio GA (2020) A numerical investigation of the geometric parametrisation of shock control bumps for transonic shock oscillation control. *Fluids* 5(2):46
- Giannelis N, Vio G, Levinski O (2017) A review of recent developments in the understanding of transonic shock buffet. *Prog Aerospace Sci* 92:39–84
- Grossi F, Braza M, Hoarau Y (2014) Prediction of transonic buffet by delayed detached-eddy simulation. *AIAA J* 52:2300–2312
- Hartmann A, Feldhusen A, Schröder W (2013) On the interaction of shock waves and sound waves in transonic buffet flow. *Phys Fluids* 25(2):026101
- Hilton WF, Fowler RG (1952) Photographs of shock wave movement. *ARC R & M* 2692
- Huang J, Xiao Z, Liu J, Fu S (2012) Simulation of shock wave buffet and its suppression on an OAT15A supercritical airfoil by IDDES. *Sci China Phys Mech Astronomy* 55:260–271
- Humble RA (2009) *Unsteady Flow Organization of a Shock Wave/Boundary Layer Interaction*. Ph.D. thesis. Delft University of Technology
- Jacquin L, Molton P, Deck S, Maury B, Soulevant D (2009) Experimental study of shock oscillation over a transonic supercritical profile. *AIAA J* 47:1985–1994
- Jones B (1936) Measurement of profile drag by the pitot-traverse. Technical report. *ARC RM1688*
- König B, Patzold M, Lutz T, Kramer E, Rosemann H, Richter K, Uhlemann H (2009) Numerical and experimental validation of three dimensional shock control bumps. *J Aircraft* 46:675–682
- Lagemann E, Brunton S, Schröder W, Lagemann C (2024) Towards extending the aircraft flight envelope by mitigating transonic airfoil buffet. *Nat Commun* 15:5020
- Lee BHK (1990) Transonic buffet on a supercritical aerofoil. *Aeronautical J* 94:143–152
- Lee BHK (1992) Effects of trailing-edge flap on buffet characteristics of a supercritical airfoil. *J Aircraft* 29:93–100
- Liu S, Xu J, Yu K (2017) McCormack's technique-based pressure reconstruction approach for pIV data in compressible flows with shocks. *Experiments Fluids* 58:1–22
- Mayer R, Lutz T, Krämer E (2018) Numerical study on the ability of shock control bumps for buffet control. *AIAA J* 56:1978–1987
- Meier HU (2010) *German Development of the Swept Wing: 1935–1945*. AIAA
- Milholen W, Owens L (2005) On the application of contour bumps for transonic drag reduction (invited). In: *AIAA 2005-46243rd AIAA Aerospace Sci Meet Exhibit*, 10-13 January, Reno, Nevada
- Ogawa H, Babinsky H, Patzold M, Lutz T (2008) Shock-wave/boundary-layer interaction control using three-dimensional bumps for transonic wings. *AIAA J* 46(6):1442–1452
- Pearcey H (1955) Some effects of shock-induced separation of turbulent boundary layers in transonic flow past aerofoils. In: *Proc N.P.L. Symposium Boundary Layer Effects Aerodynamics*

- Piccola J (2012) Flight Test Guide For Certification Of Transport Category Airplanes. Technical report. Federal Aviation Administration, Advisory Circular AC 25-7C
- Raffel M, Willert C, Scarano F, Kahler C, Wereley S, Kompenhans J (2018) Particle Image Velocimetry A Practical Guide. Springer
- Ragni D, Ashok A, Oudheusden B, Scarano F (2009) Surface pressure and determination of a transonic aerofoil based on particle image velocimetry. *Measure sci technol* 20:074005
- Ragni D, Schrijer FFJ, van Oudheusden BW, Scarano F (2011) Particle tracer response across shocks measured by PIV. *Experiments in Fluids* 50:53–64
- Ren K, Chen Y, Gao C, Zhang W (2020) Adaptive control of transonic buffet flows over an airfoil. *Phys Fluids* 32:096106
- Sciacchitano A, Scarano F (2014) Elimination of PIV light reflections via a temporal high pass filter. *Measure Sci Technol* 25(8):084009
- Szubert D, Grossi F, Jimenez Garcia A, Hoarau Y, Hunt J, Braza M (2015) Shock-vortex shear-layer interaction in the transonic flow around a supercritical airfoil at high Reynolds number in buffet conditions. *J Fluids Struct* 55:276–302
- Tagliabue A, Scharnowski S, Kähler C (2017) Surface pressure determination: a comparison between piv-based methods and psp measurements. *J Visualization* 20:581–590
- Tian Y, Gao SQ, Liu PQ, Wang JJ (2017) Transonic buffet control research with two types of shock control bump based on rae2822 airfoil. *Chinese J Aeronautics* 30:1681–1696
- Tijdeman H (1977) Investigations of the transonic flow around oscillating airfoils. Ph.D. thesis. Delft University of Technology
- van Oudheusden BW (2008) Principles and application of velocimetry-based planar pressure imaging in compressible flows with shocks. *Experiments Fluids* 45:657–674
- van Oudheusden BW (2013) Piv-based pressure measurement. *Measure Sci Technol* 24:032001
- van Oudheusden BW, Scarano F, Casimiri EWF (2006) Non-intrusive load characterization of an airfoil using piv. *Experiments Fluids* 40:988–992
- van Oudheusden BW, Scarano F, Roosenboom E, Casimiri E, Souverein L (2007) Evaluation of Integral forces and pressure fields from planar velocimetry data for incompressible and compressible flows. *Experiments Fluids* 43:153–162

Publisher's Note Springer Nature remains neutral with regard to jurisdictional claims in published maps and institutional affiliations.